

Shape Memory and Underwater Superelastic MOF@Cellulose Aerogels for Rapid and Large-capacity Adsorption of Metal Ions

Meng Wang (✉ wmbjfu@163.com)

Qilu University of Technology <https://orcid.org/0000-0003-1691-7617>

Lupeng Shao

Qilu University of Technology

Mengying Jia

Shandong Jianzhu University

Research Article

Keywords: Super-elastic, Cellulose, MOF, Aerogels, Adsorption

Posted Date: May 5th, 2022

DOI: <https://doi.org/10.21203/rs.3.rs-1460350/v1>

License:  This work is licensed under a Creative Commons Attribution 4.0 International License.

[Read Full License](#)

1 **Shape Memory and Underwater Superelastic MOF@Cellulose Aerogels for Rapid and Large-**
2 **capacity Adsorption of Metal Ions**

3 *Meng Wang,^{a*} Lupeng Shao^a and Mengying Jia^{b,*}*

4 ^a State Key Laboratory of Biobased Material and Green Papermaking, Qilu University of Technology,
5 Shandong Academy of Sciences, Jinan, 250353, China

6 ^b School of Information and Electrical Engineering, Shandong Jianzhu University, Jinan 250101, China.

7 a* Email: wmbjfu@163.com

8 b* Email: jmybl2016@163.com

9
10 **Abstract** Cellulose aerogels (CA) have been used in widespread areas, such as absorbents, thermal
11 insulation material and medical material. Herein, a robust strategy to fabricate cellulose aerogels by
12 combining cellulose nanofibers with PVA “glue”. The CA not only had a robust chemical-bond cross-
13 link network, but also had a strong H-bond, which enhanced underwater mechanical properties. Moreover,
14 the compressible CA provided a large number of nucleation sites for the growth of Metal-organic frame
15 (MOF) nanoparticles (ZIF-67 and ZIF-8) through interface self-assemble. The obtained aerogels with a
16 low density of 9.8-11.2 mg cm⁻³ and highly porous of 99.4-99.5% possessed excellent mechanical
17 properties both in air and underwater. The adsorption capacities of the MOF@CA for Pb²⁺ and Cu²⁺ are
18 up to 105.21 mg g⁻¹ and 54.78 mg g⁻¹, respectively. The novel MOF@CA adsorbents with excellent
19 mechanical properties display application prospects in the removal of heavy metals from wastewater.

20
21 **Keywords** Super-elastic, Cellulose, MOF, Aerogels, Adsorption

22
23 **Introduction**

24 With the development of industry, environmental pollution becomes an increasingly serious issue
25 (Ali and Khan 2017). As one of the most common pollutants, heavy metals accumulate in aquatic
26 organisms and human bodies, causing great harm to public health and environmental health (Ali et al.
27 2019). The removal of these heavy metals such as Hg²⁺, Ni²⁺, Cd²⁺, Cr⁵⁺, Pb²⁺ and Cu²⁺ from polluted
28 wastewater had become the focus of environmental problems in the world. Generally speaking, the
29 methods for removing heavy metal ions from water included chemical precipitation, ion exchange,
30 membrane filtration, flocculation, and adsorption (Peng and Sun 2010). The adsorption as the preferred
31 method can remove multiple icons simultaneously because it does not require complex chemical
32 reactions, which is considered to be one of the most promising treatment methods (Jia et al. 2002). To
33 date, various absorbent materials had been used for water treatment including zeolites. (Fei et al. 2012).
34 clays (Chan et al. 2015), polystyrene (Tran et al. 2020), activated carbon (Chen and Lin 2001) etc.
35 Nevertheless, these absorbent materials were difficult to be widely used because of the poor adsorption
36 capacity, non-degradation and expensive cost.

37 Cellulose is one of the most abundant polymers in nature, which is biocompatible, economical and
38 biodegradable (Zhao et al. 2020). Cellulose aerogels (CA) are prepared from cellulose solution or
39 nanocellulose as the substrate, which have the advantages of high porous and low density, and have broad
40 application prospects in many fields of adsorption, catalysis, drug loading and so on (Wang et al. 2017).

41 However, the poor underwater mechanical properties of CA have greatly limited the application in the
42 fields of adsorption (Huang et al. 2020). This was ascribed to the weak hydrogen bond forces between
43 CA molecular chains, where the irreversible damage may occur during deformation. Moreover, the
44 sensitivity of hydrogen bonding interactions between the cellulose hydroxyl groups and pollutant
45 molecules in aqueous environment, results in the insufficient affinity of cellulose-based adsorbents,
46 which limits their practical applications (Song et al. 2020).

47 Metal-organic frameworks (MOF) are emerging porous materials consisting of metal-containing
48 nodes and organic ligands connected by coordination bonds, which have a large specific surface area and
49 have been used as adsorbents for the removal of contaminants from the aqueous environment (Furukawa
50 et al. 2013). Although MOFs have many unique properties, including abundant pore structures and a
51 variety of functional ligands, their applied performance is still limited by intrinsic fragility and powdered
52 crystalline state, as well as unsatisfied stability and processability (Wang et al. 2019). Recently, several
53 reports on the composite of MOF nanoparticles with cellulose had been published (Zhou et al. 2019, Da
54 Silva Pinto et al. 2012, Bo et al. 2018). The composite had excellent properties of both MOF and cellulose,
55 with better removal of organic dye molecules and heavy metal ions from contaminated aqueous solution.
56 However, due to the weak interaction between particles and the inherent rigidity of MOFs, the composite
57 aerogels also lack sufficient flexibility and robustness. Hence, it still a huge challenge for the fabrication
58 of flexible and shape controllable MOF@cellulose aerogels.

59 Here, we reported a new strategy to fabricate the CA by using crosslinking PVA chains as “glue” to
60 bond cellulose nanofibers together. The abundant active sites of CA provided nucleation sites of MOF
61 (ZIF-67 and ZIF-8) nanoparticles. The prepared MOF@CA shown excellent water absorption, shape
62 recovery property under the water and high adsorption property. We had characterized the morphology,
63 chemical and mechanical properties of the aerogels both in the air and under the water. Besides, the
64 adsorption and desorption properties of the aerogels were evaluated. By using Pb^{2+} and Cu^{2+} as model
65 contaminants, the adsorption performance, as well as its selectivity and reusability, were investigated by
66 batch adsorption experiments. Further, the adsorption mechanism was explored by fitting the
67 experimental data of adsorption kinetics and isotherms to different adsorption models. This study
68 providing a new prospect for eco-friendly and sustainable adsorption materials, and developing a new
69 way for the development and utilization of cellulose.

70

71 **Method**

72

73 **Materials and chemicals**

74

75 A softwood kraft pulp was provided by Northwood Pulp (Canada). 2, 2, 6, 6-tetramethylpiperidine-
76 1-oxyl (TEMPO) was purchased from Sigma-Aldrich. Sodium hydroxide (NaOH), sodium bromide
77 (NaBr), sodium hypochlorite (NaClO 12%), polyvinyl alcohol (PVA, MW=17 000±50), citric acid
78 (CCA), methyl alcohol, phosphoric acid (H_3PO_4 , 80 wt%), 2-methylimidazole, $Zn(NO_3)_2 \cdot 6H_2O$,
79 $Co(NO_3)_2 \cdot 6H_2O$, $Pb(NO_3)_2$, and $Cu(NO_3)_2 \cdot 3H_2O$ were all purchased from MACKLIN (Shanghai). All
80 chemicals were laboratory grade and used without further purification. Ultrapure water ($18.2 M\Omega \cdot cm$)

81 was produced by a Heal Force purification system and used to prepare all aqueous solutions.

82 *Preparation of the TEMPO-oxide cellulose nanofibers (TOCN)*

83 TOCN was prepared by oxidizing pulp according to our previous work (Wang et al. 2019). In brief,
84 the softwood kraft pulp was thoroughly washed with deionized water and dried in the oven at 100 °C for
85 12h. TEMPO (0.032 g) and NaBr (0.2 g) were dissolved in softwood kraft pulp suspension (1wt%, 200
86 mL). The TEMPO-mediated oxidation was initiated by adding the desired amount of the NaClO solution
87 (10 mmol) and stirred at room temperature. The pH was maintained at 10 by adding 0.5 M NaOH using
88 a pH meter until no NaOH consumption was observed. After stirring for 10 h, the suspension was
89 thoroughly washed with water via centrifugation. Then the TEMPO-oxidized cellulose suspension was
90 fibrillated by a high-pressure homogenizer at 100 MPa for 5 cycles. The carboxylate content of the
91 nanofibers was examined using an electric conductivity titration process and found to be 0.052 mmol/g.

92 *Fabrication of TOCN/PVA aerogels (TPA)*

93 PVA (0.1 g, 0.2 g, 0.3 g) was dissolved in TOCN suspensions (0.5 wt%, 100 mL) using a magnetic
94 stirrer at 90 °C for 2h. Then the suspensions were cooled down to room temperature. Subsequently, CCA
95 (1.2g) and 1.2 mL (H₃PO₄) were added to the suspension with continuous stirring for 1h. The suspensions
96 were added to a plastic beaker and put in liquid nitrogen for 5 min. After the complete freeze, the samples
97 were freeze-dried at a freezer dryer to obtain the aerogel. Consequently, the aerogels were heated in an
98 oven at 60 °C for 2h to achieve the crosslinking reaction between PVA and CCA. Then the samples were
99 washed thoroughly with deionized water and dried at room temperature. The obtained TOCN/PVA
100 aerogel was named TPA.

101 *Fabrication of MOF self-growing aerogels*

102 The TPA was immersed in the corresponding solutions of ligand precursors in alcohol for the growth
103 of ZIF-8 and ZIF-67 under specific experimental. In detail, the prepared TPA were soaked in 40 mL
104 methanol containing 0.8g Zn(NO₃)₂ 6H₂O solution for 10 min, and then 40 mL methanol containing 1.76
105 g 2-methylimidazole was slowly added into the above solution. Then the aerogels were squeezed
106 repeatedly until the two solutions were well mixed. Subsequently, the mixture was aged at room
107 temperature for 12h to grow ZIF-8 particles. The sample was obtained after being washed with ethanol
108 and freeze-dried (-56 °C, <20 Pa) at a freeze dryer. Similarly, the ZIF-67 particles were grown onto the
109 surface of TPA by simple impregnation. In brief, the TPA was immersed in 40 mL methanol containing
110 0.416g Co(NO₃)₂ 6H₂O solution for 10 min, and 40 mL methanol containing 2.0g 2-methylimidazole
111 was slowly added into the above solution. The mixture was aged at room temperature for 12h and freeze-
112 dried to obtain the aerogel. The resulting ZIF-8@TPA and ZIF-67@TPA were abbreviated as TPAZ-8
113 and TPAZ-67, respectively.

114 *Characterization*

115 The TOCN were collected using carbon film-covered copper grids and observed using transmission
116 electron microscopy (TEM, Talos F200X) at an accelerator voltage of 80 kV. The surface morphology of
117 the samples was observed by scanning electron microscopy (SEM, Hitachi S4800) at an accelerator
118 voltage of 15 kV. The chemical structures of the samples were studied by a Fourier-transform infrared
119 (FTIR) spectrometer (Nicolet 5700, Thermo Fisher, America). The nitrogen adsorption and desorption
120 isotherms were recorded with a Micrometrics ASAP 2020 analyzer. Pore size distribution and specific

121 surface area were calculated via Barrett-Joyner-Halenda (BJH) and Brunauer-Emmett-Teller (BET)
122 methods, respectively. The X-ray diffraction (XRD) measurement was performed using a D8-Advance
123 with Ni-filtered Cu-K α radiation ($\lambda = 0.15406$ nm), with a sweeping range of $5 \sim 60^\circ$ and scanning speed
124 of 2° min^{-1} . Raman spectra analysis was conducted by a Renishaw in Via Reflex Raman Spectrometer.
125 X-ray photoelectron spectroscopy (XPS) analysis was performed with an ESCALAB 250
126 Xiphotoelectron spectroscopy using a monochromic Al X-ray source.

127 *Mechanical properties*

128 The mechanical characterizations (uniaxial compression) of aerogels were measured using an
129 electronic universal testing machine (UTM6530, Shenzhen Suns Technology Co., Ltd). The cylindrical
130 samples were put on the platform and examined at a speed of 50 mm/min.

131 *Adsorption evaluation of the aerogels*

132 The Pb $^{2+}$ and Cu $^{2+}$ were used to evaluate the adsorption capacity of the aerogels in aqueous solution.
133 First of all, the Pb(NO $_3$) $_2$ and Cu(NO $_3$) \cdot 3H $_2$ O were dissolved in deionized water to prepare a 200 mg L $^{-1}$
134 solution, and the pH of the solution was measured to be 5.0 ± 0.2 for Pb $^{2+}$ and 5.2 ± 0.2 for Cu $^{2+}$,
135 respectively. The aerogels (3 mg) were incubated in 5 mL of metal ion solutions in a shaker at 25°C. The
136 concentrations of metal ions were measured with Sequential Plasma Spectrometer (iCAP PRO ICP-OES
137 Duo) at wavelengths of 220.351 and 327.396 nm for Pb $^{2+}$ and Cu $^{2+}$, respectively.

138 *Desorption experiment of aerogels*

139 The deionized water, methanol, 0.1 M HNO $_3$, and 0.1 M HCl were used as an eluent to treat the
140 adsorbed saturated aerogels. The saturated aerogels (3 mg) with 50 mL of aqueous solutions were
141 oscillated in a shaker at 25°C for 2h. Then the samples were washed with deionized water until neutral
142 and drying at 50 °C for adsorption experiments. The regeneration rate calculation (R) formula is as follow:

$$143 \quad R = \frac{q_t}{q_0} * 100\% \quad (1)$$

144 Where q_t (mg g $^{-1}$) is adsorption capacity after regeneration t times (t), q_0 (mg g $^{-1}$) is adsorption
145 capacity before regeneration.

146

147 **Results and discussion**

148

149 Fabrication and structure characterization

150

151 The fabrication process of TPAs was illustrated in Fig. 1a. The TOCN and PVA suspensions
152 containing CCA were freeze-dried to obtain the aerogels. The freshly obtained aerogels with some
153 viscosity were difficult to recover to their original shape after compression because of the weak hydrogen
154 bonds among TOCN and PVA molecular chains and CCA. Subsequently, the resulting aerogels were
155 heating in the air (60 °C for 2 h) to realize the robust crosslinking esterification between TOCN and PVA
156 and CCA. At last, the aerogels were immersed in the ions and organic ligands solution for growing the
157 MOF particles uniformly (Fig. S1). The obtained aerogels with a low density of 9.8—11.2 mg cm $^{-3}$ could
158 steadily stand on the soft grass.

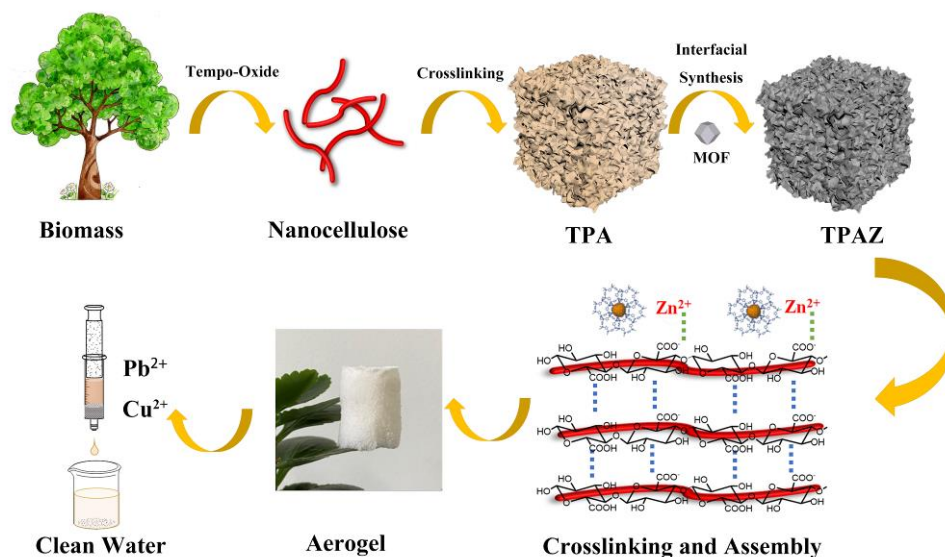


Fig.1 Schematic illustrations of the fabrication process of TPAZ

159

160

161

162

163

164

165

166

167

168

169

170

171

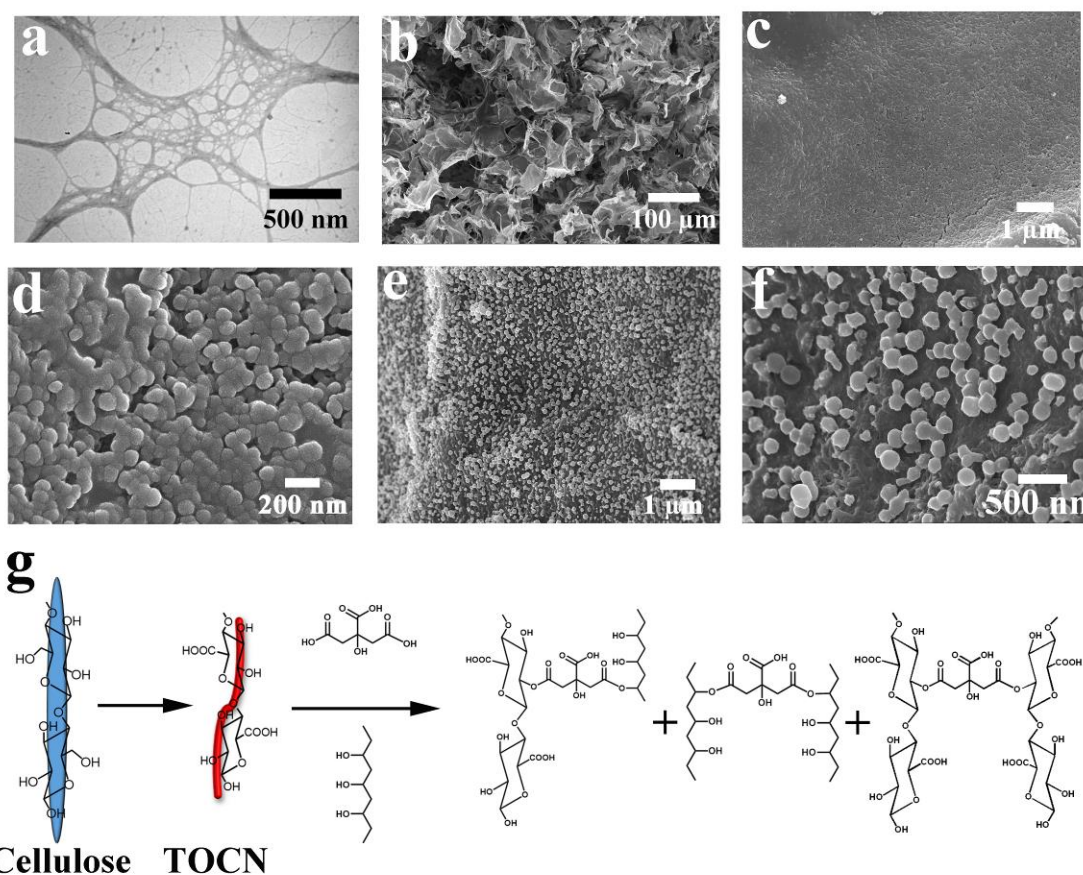
172

173

174

175

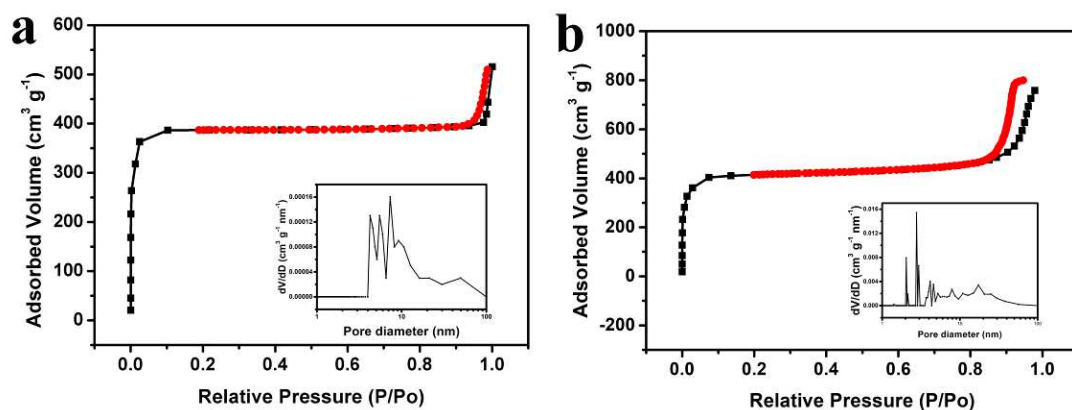
As shown in Fig. 2a, the original cellulose was oxidized by TEMPO and the hydroxyl group of C6 was oxidized to carboxyl group (Isogai et al. 2011) etc. After homogeneous, the TOCN possesses a high aspect ratio with a diameter of 5-15 nm and a length of 0.5-1.5 μm . Mostly cellulose nanofibers were woven together to form a network, which can form a robust aerogel skeleton (Wang et al. 2017). As illustrated in Fig. 2b, the TPA aerogels have a rich porous structure with a diameter of 10-20 μm , which was ascribed to the sublimation of ice crystals in the aerogel during the freeze-drying process. Furthermore, there is no single TOCN that can be seen in the SEM image because of the crosslinking of the PVA, TOCN and CCA. As illustrated in Fig. 2g, the TOCN, PVA and CCA may form these ester bonds during the heating process. When the aerogels were immersed in metal ions (Zn^{2+} , Co^{2+}) solution, the metal ions with positive charge rapidly interacted with the carboxyl groups on the surface of aerogels by electrostatic action. Then the ZIF-8 or ZIF-67 were nucleated at the surface of the aerogels by interface self-growing. As shown in Fig.2c and d, the ZIF-8 nanoparticles with a diameter of 100 nm were adhered to aerogels' surface via hydrogen bonding and ionic interactions, while the ZIF-67 grows on the surface of aerogel in the same way (Zhu et al. 2018). The loading mass of crystals within the aerogels can be easily adjusted from 10-80% by controlling the initial concentration of ions and organic ligands.



176

177 **Fig. 2 a** TEM image of TOCN, **b** SEM image of the TPA. **c, d** SEM images of TPAZ-8 at different
 178 magnifications. **e, f** SEM images of TPAZ-8 at different magnifications. **g** The mechanism and products
 179 of the reaction between TOCN, PVA and CCA.

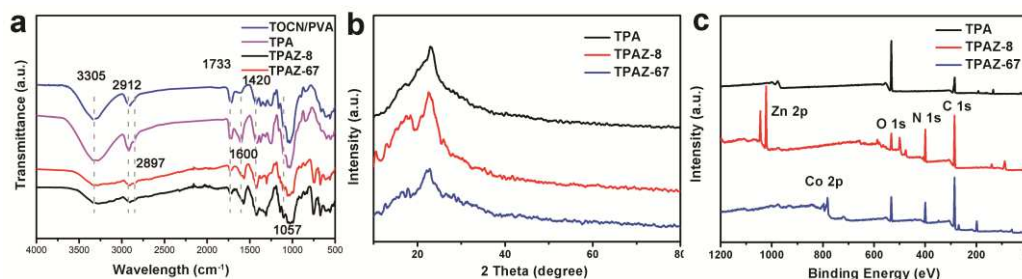
180 As shown in Fig. S2, the N_2 uptake at high relative pressures of TPA was dramatically increased
 181 and an obvious hysteresis loop was observed, revealing that there were abundant mesopores and
 182 macropores in the aerogels. These mesopores and macropores were derived from the cellulose aerogels
 183 after the ice crystal sublimation, which provided plenty of locations for the growth of MOF nanoparticles.
 184 N_2 adsorption-desorption isotherms and the corresponding pore size distribution of the TPAZ-8 and
 185 TPAZ-67 were shown in Fig. 3. After the growth of MOF nanoparticles, the aerogels possess three types
 186 of pore structure including micropores, mesopores and macropores. The specific surface area of TPA is
 187 $43.63 \text{ m}^2 \text{ g}^{-1}$, and the TPAZ-8 and TPAZ-67 are up to $90.21 \text{ m}^2 \text{ g}^{-1}$ and $220.57 \text{ m}^2 \text{ g}^{-1}$, respectively. The
 188 increase of specific surface area of TPAZ mainly comes from porous MOF particles. The open multi-
 189 pore structure, high surface area and abundant hydroxyl are beneficial for the rapid entry of wastewater
 190 into the pores and the adsorption of metal ions.



191

192 **Fig. 3** N₂ adsorption-desorption isotherms and pore size distribution of **a** TPAZ-8 and **b** TPAZ-67.

193 The chemical structure and possible interaction of TPA and TPAZ-8, TPAZ-67 were investigated by
 194 FT-IR, XPS, and XRD. The FT-IR spectra showed the expected signals from all the components within
 195 the aerogels. As shown in Fig. 4a, the TOCN/PVA mixture exhibits several absorption bands at 3305
 196 cm⁻¹, 1600 cm⁻¹, and 1057 cm⁻¹, which are attributed to the O-H, C=O, and C-O stretching vibrations
 197 from cellulose and PVA, respectively (Ha et al. 2015). Besides, character peaks appearing at 2897 cm⁻¹
 198 and 1420 cm⁻¹ correspond to the C-H stretching and bending of the -CH₂ groups of cellulose,
 199 respectively (Zhang et al. 2015). The carboxyl (1733 cm⁻¹) mainly came from C6 of TEMPO oxide
 200 cellulose (Isogai et al. 2011). After heating, the intensity of ester bond (1600 and 1733 cm⁻¹) of TPA was
 201 remarkably strengthened, indicating that a large number of ester bonds were formed during the heating
 202 process (Fig. 2g). Moreover, a slight shift of the hydroxyl peak was observed from 3305 to 3296 cm⁻¹,
 203 which might attribute to forming intermolecular hydrogen bonding among the TOCN, PVA and CCA.
 204 After the growth of ZIF-8, a sharp peak at 1140 cm⁻¹ was formed, which was identified as C-N bonds
 205 in ZIF-8 (Hu et al. 2011). Similarly, after the growth of ZIF-67, new peaks at 1576 and 422 cm⁻¹ appeared,
 206 corresponding C=N and Co-N vibrations of ZIF-67, respectively (Yang et al. 2018). The formation of
 207 the MOF nanoparticles was confirmed by the existence of all the peaks related to ZIF-8 and ZIF-67 in
 208 its FT-IR spectrum.



209

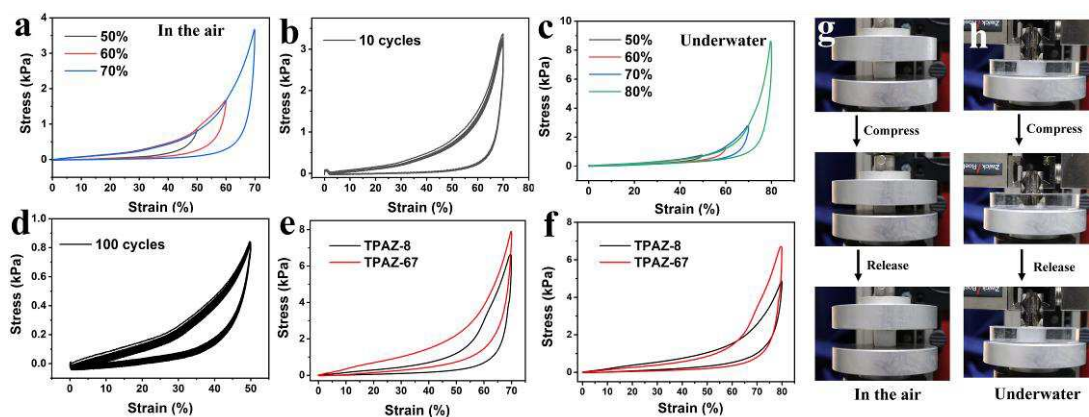
210 **Fig. 4 a** FTIR spectra of the TOCN/PVA mixture, TPA, TPAZ-8, and TPAZ-67. **b** XRD and **c** XPS spectra
 211 of TPA, TPAZ-8 and TPAZ-67, respectively.

212 The TOCN displayed three diffraction peaks at 14.7°, 16.8° and 22.7°, which corresponded to the
 213 (1-10), (110) and (200) planes of cellulose I, respectively (Oh et al. 2005). After heating, the diffraction
 214 peaks of PVA (11.5, 19.6, 22.5 and 40.2°) nearly disappeared, which indicated that the CCA strongly
 215 interacted with the hydroxide radical of PVA (Fig. 4b). The characteristic peaks of ZIF-8 (Yichang 2011)
 216 and ZIF-67 (Pan et al. 2011) in the XRD pattern of aerogels again confirm the formation of MOF in the

217 aerogels. Moreover, the XPS results provided the surface chemistry of the TPA, TPAZ-8 and TPAZ-67.
 218 As shown in Fig. 4c, TPA has two peaks at 285 and 532 eV corresponding to C 1s and O 1s. Compared
 219 to TPA, the TPAZ-8 has a peak at 400 and 1023 eV, corresponding to N 1s and Zn 2p from ZIF-8. There
 220 are two major peaks of Co 2p_{3/2} (781.2 eV) and Co 2p_{1/2} (796.4 eV) in the TPAZ-67, which corresponded
 221 to the characteristic of ZIF-67 (Yang et al. 2018).

222 Mechanical properties

223
 224
 225 As shown in Fig. 5a, 5g and Movie S1, the TPA shown excellent compressible property, which can
 226 completely recover to its original height at 70% compression strain in the air after the stress was removed.
 227 The TPA was subject to cyclic compression tests at different stains (50%, 60%, 70%). As illustrated in
 228 Fig. 5b, the loading stress-strain curve can be divided into three regions, which is typical tree-region
 229 curves of traditional foam materials. In an elastic region ($\varepsilon < 30\%$), the stress was increased linearly with
 230 the compressive stress. In the following yield region ($30\% < \varepsilon < 60\%$), the compressive stress gradually
 231 increased with the strain because of the elastic bending of the skeleton of the aerogels. The last
 232 densification region ($\varepsilon > 60\%$) was marked by a rapid increase of compressive stress, owing to the
 233 densification of the pore. Moreover, the stress-strain curve at 10th almost coincided with the 1st (Fig.
 234 5c), showing excellent fatigue-resistant property. After the growth of MOF, the compress stress increased
 235 under the same strain (Fig. 5e), which was ascribed to the adhesion of a layer of rigid MOF particles on
 236 the surface of TPA. Moreover, both the TPAZ-67 and TPAZ-8 had excellent compressible performance,
 237 which can recover to its original height at 70% strain (Fig. 5e).



238
 239 **Fig. 5** **a** Stress-strain curves of TPA under different stains in the air. **b** Stress-strain curves of TPA at 10th
 240 cycles at 70% strain in the air. **c** Stress-strain curves of TPA under different stains under the water. **d**
 241 Stress-strain curves of TPA at 100th cycles at 50% strain under the water. **e** Stress-strain curves of TPAZ-
 242 8 and TPAZ-67 at 70% strain in the air. **f** Stress-strain curves of TPAZ-8 and TPAZ-67 at 80% stain under
 243 the water. Compression and release process of the TPA **g** in the air and **h** under the water.

244 Even underwater, the TPA still exhibits excellent elasticity and fatigue-resistance. As shown in
 245 Movie S2, the TPA was immersed in a glass of water, and mostly absorbed water could be easily removed
 246 by simple squeezing methods. Once the squeezed TPA was in contact with water, it could reabsorb water
 247 instantaneously and return to the original shape in a very short time of 1.5 s, showing excellent water-
 248 activated shape recovery. This may ascribe to the functional crosslinked PVA polymer that could be acted

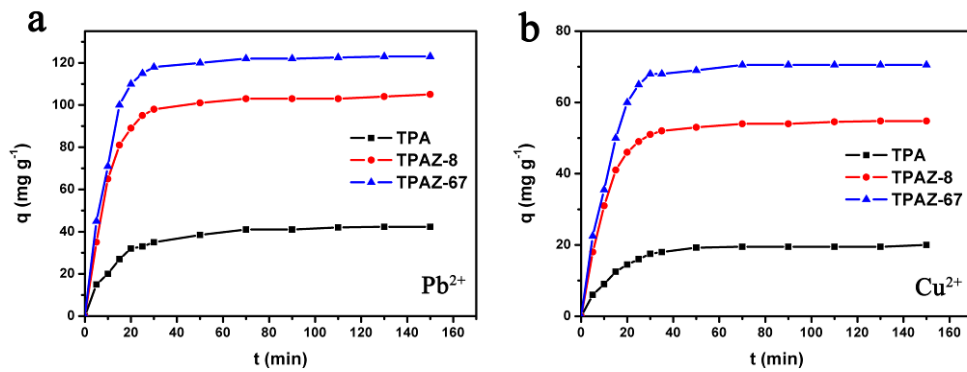
249 as the glue which could effectively bond the TOCN to endow the TPA with high mechanical elastic. As
 250 shown in Fig. 5c and Movie S3, the TPA was subject to cyclic compression tests at different stains under
 251 the water. The stress-strain curves of the TPA underwater are similar to the compression process in air,
 252 which can be divide into three regions. However, the TPA showed better compressibility (80%) and
 253 fatigue resistance (80%, 100 cycles) than in the air. After the growth of MOF, the excellent mechanical
 254 properties are still preserved in the TPAZ-8 and TPAZ-67 (Fig. 5f).

255

256 Adsorption property and adsorption mechanism of the aerogels

257

258 Pb^{2+} and Cu^{2+} are common heavy metal ions in wastewater. Here, Pb^{2+} and Cu^{2+} were used as a
 259 model cationic adsorbate (Fig. 6) to investigate the static adsorption property. The adsorption capacity
 260 of Pb^{2+} for the TPA, TPAZ-8 and TPAZ-67 were 42.3 mg g^{-1} , 105 mg g^{-1} and 123 mg g^{-1} , respectively.
 261 For Cu^{2+} , the adsorption of TPA, TPAZ-8 and TPAZ-67 were 20.12 mg g^{-1} , 54.78 mg g^{-1} and 70.53 mg g^{-1} ,
 262 respectively. Such high adsorption capacity and distribution coefficient surpassed those of most of
 263 the previous absorbent materials (Chen et al. 2010, Chen et al. 2009, Gurgel et al. 2008). Moreover, all
 264 the samples showed a high adsorption rate at the initial stage of adsorptions (0-30 min), which may be
 265 due to the high wettability and porosity of the aerogels. The TPAZ-8 and TPAZ-67 showed more
 266 efficient adsorption than TPA, which was ascribed to the high porousness of ZIF-8 and ZIF-67.



267

268 **Fig. 6** Adsorption capacities of **a** Pb^{2+} and **b** Cu^{2+} on TPA, TPAZ-8 and TPAZ-67.

269

270 The adsorption model is an important tool to describe the adsorption behavior and mechanism. In
 271 this study, two typical kinetic models, pseudo-first-order (Eq.2) and pseudo-second-order models (Eq.
 272 3), were used for fitting adsorption kinetic curves.

272 The pseudo-first-order model:

273

$$\ln(q_e - q_t) = \ln q_e - k_1 t \quad (2)$$

274

274 The pseudo-second-order kinetic model:

275

$$\frac{t}{q_t} = \frac{1}{k_2 q_e^2} + \frac{1}{q_e} t \quad (3)$$

276

276 The Langmuir isotherm model:

277

$$\frac{C_e}{q_e} = \frac{1}{q_m K_L} + \frac{C_e}{q_m} \quad (4)$$

278

278 The Freundlich isotherm model:

279

$$\ln q_e = \frac{1}{n} \ln C_e + \ln K_F \quad (5)$$

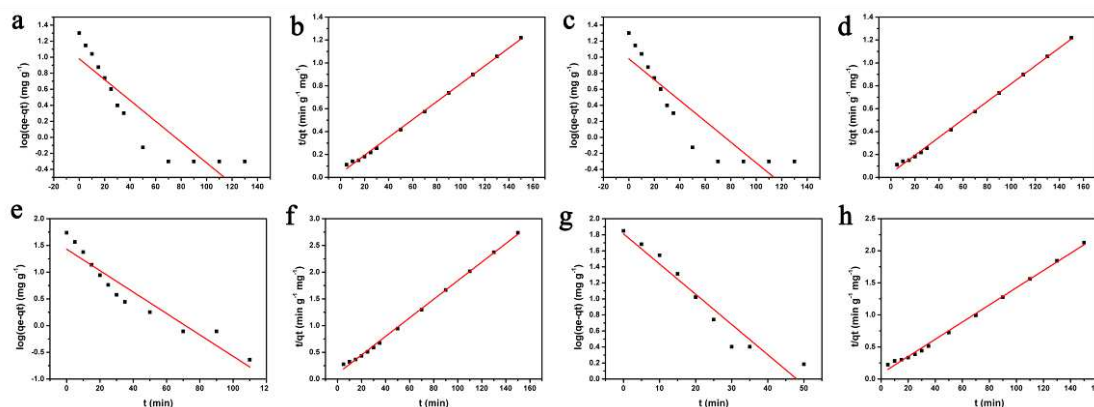
280 Where q_e (mg g^{-1}) and q_t (mg g^{-1}) are the adsorption equilibrium and the adsorption amount at time
 281 t , respectively; k_1 (min^{-1}) and k_2 ($\text{g mg}^{-1} \text{min}^{-1}$) are the pseudo-first-order and pseudo-second-order rate
 282 constants, respectively; C_e is the equilibrium concentration of metal ions in aqueous solution ($\text{mg}\cdot\text{L}^{-1}$);
 283 q_m and K_L (L mg^{-1}) are the Langmuir constants related to q_e for a complete monolayer and energy of
 284 adsorption, respectively; K_F (mg g^{-1}) and n are the Freundlich constants that indicate the adsorption
 285 capacity and adsorption intensity, respectively.

286 As shown in Table 1 and Fig. 7, values of R^2 are generally higher than R^1 , indicating the pseudo-
 287 second-order model fitted the experimental data of all samples better compared to the pseudo-first-order
 288 model. Further illustrates that the adsorption process was mainly controlled by the chemical adsorption
 289 mechanism (Yan et al. 2015).

290 **Table 1.** Calculated constants of pseudo-first-order and pseudo-second-order models for Cu^{2+} and
 291 Pb^{2+} adsorption on different adsorbents

Metal ion	Sample	q_e (exp.) mg/g	k_1 (min^{-1})	R^1	k_2 ($\text{g mg}^{-1} \text{min}^{-1}$)	R^2
Cu^{2+}	TPA	20.10	-0.02088	0.87514	0.0078	0.99812
	TPAZ-8	54.78	-0.02005	0.90855	0.01737	0.99798
	TPAZ-67	70.53	-0.03772	0.9281	0.01341	0.99624
Pb^{2+}	TPA	42.32	-0.01073	0.919	0.02197	0.99924
	TPAZ-8	105.51	-0.01401	0.82497	0.00916	0.99833
	TPAZ-67	123.07	-0.02088	0.87514	0.0078	0.99812

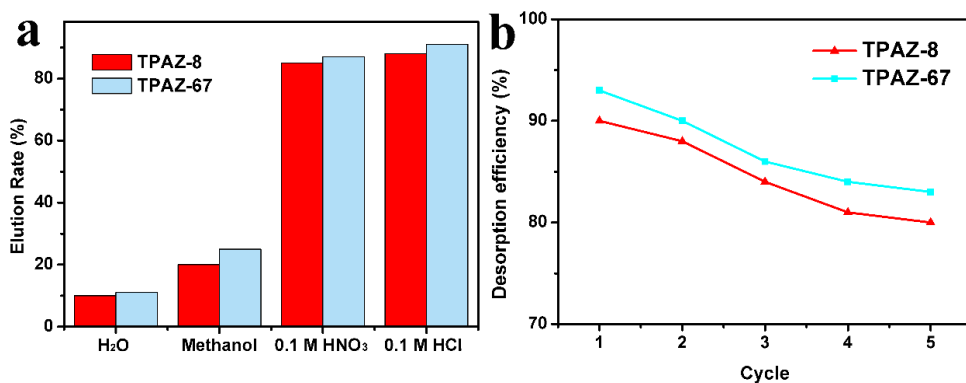
292



293

294 **Fig. 7** Pseudo-first-order kinetic plots of **a** TPAZ-8 and **c** TPAZ-67 for Cu^{2+} . Pseudo-first-order kinetic
 295 plots of **e** TPAZ-8 and **g** TPAZ-67 for Pb^{2+} . Pseudo-first-order kinetic plots of **b** TPAZ-8 and **d** TPAZ-67
 296 for Cu^{2+} . Pseudo-first-order kinetic plots of **f** TPAZ-8 and **h** TPAZ-67 for Pb^{2+} .

297 As shown in Fig. 8a, the elution efficiency of different eluents for TPAZ-8 and TPAZ-67 were tested.
 298 The elution efficiency of the TPAZ-8 and TPAZ-67 is about 10% in water, while is about 90% in 0.1 M
 299 of HCl. Therefore, 1 M HCl was selected as the eluent and the cyclic adsorption capacity as illustrated
 300 in Fig. 8b. After five times of adsorption-desorption, the adsorption efficiency of TPAZ-8 and TPAZ-67
 301 were still maintained at 80% and 83%, respectively, indicating that the aerogels had excellent
 302 repeatability and potential application in the field of adsorption.



303

304

Fig. 8 a The elution efficiency of different elution solutions for TPAZ-8 and TPAZ-67. **b** Recycle adsorption performance of TPAZ-8 and TPAZ-67 over five successive cycle adsorption-desorption cycles.

305

306

The aerogels possess shape-controllably, fast recovery, and rapid adsorption kinetics, which provides convenience for many special cases. As shown in Fig. 9 and Movies S4, the cylindrical aerogels were packed into syringes to filter contaminants from water. After three suction and extrusion at a flow rate of 6 L h⁻¹, the concentration was reduced by 85%. Furthermore, in contrast with other aerogels, the solution in the resulting aerogels can be squeezed sufficiently accelerating the discharge of the filtrate. Moreover, the strong interaction between MOF and cellulose aerogels ensured minimal MOF loss during repeated adsorption, showing excellent adsorption stability.

307

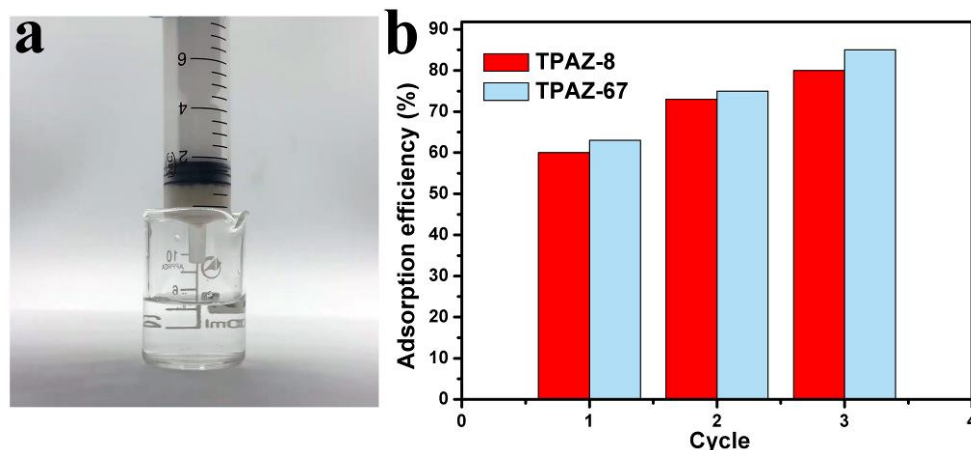
308

309

310

311

312



313

314

Fig. 9 a A simple adsorption device assembled with a syringe. **b** The removal rate of Cu²⁺ in water after three filtrations.

315

316

317

Conclusion

318

319

In this study, ultralight and under-water elastic cellulose aerogels were successfully fabricated through esterification crosslink of the cellulose nanofiber with PVA. The aerogels not only offered excellent mechanical flexibility and high porosity, but also provided abundant nucleation sites for growing MOF crystals. The resulting MOF@ cellulose aerogels with high porosity up to 90% and a low density of 9.8-11.2 mg cm⁻³, showing high adsorption capacity for mental icons and rapid adsorption kinetics. The adsorption capacities of TPAZ-8 for Pb²⁺ and Cu²⁺ is up to 105 mg g⁻¹ and 54.78 mg g⁻¹, while the TPAZ-67 is 123 mg g⁻¹ and 70.53 mg g⁻¹. Among them, the adsorption capacity of TPAZ-67 is

325

326 better than that of TPAZ-8, because of the larger specific surface area and rational pore size distribution
327 of TPAZ-67. The kinetic studies show that the absorption of Pb^{2+} and Cu^{2+} on TPAZ can be described by
328 the pseudo-second-order model. Moreover, the shape-controllable and high elasticity of TPAZ-67 make
329 it a special filter device for water purification applications. In brief, these remarkable properties make it
330 have high potential application value in wastewater treatment and adsorption fields.

331

332 **Acknowledgements** This work was supported by the Foundation (ZZ20210105) of State Key
333 Laboratory of Biobased Material and Green Papermaking, Major Scientific and Technological
334 Innovation Project of Shandong (2019JZZY010457 and 2019JZZY020309), Innovation Pilot Project of
335 Integration of Science, Education and Industry of Shandong Province (2020KJC-ZD06).

336

337 **Competing Interests** The authors declare no conflict of interest.

338

339 **Author Contributions** All authors contributed to the study conception and design. Material
340 preparation, data collection and analysis were performed by Meng Wang, Lupeng Shao and Mengying
341 Jia. The first draft of the manuscript was written by Meng Wang and all authors commented on previous
342 versions of the manuscript. All authors read and approved the final manuscript.

343

344

345 **Reference**

346

347 Ali H, Khan E (2017) Environmental chemistry in the twenty-first century. *Environmental Chemistry*
348 *Letters* 15:329-346

349 Ali H, Khan E, Ilahi I (2019) Environmental Chemistry and Ecotoxicology of Hazardous Heavy Metals:
350 Environmental Persistence, Toxicity, and Bioaccumulation. *Journal of Chemistry* 2019:1-14

351 Bo S, Ren W, Lei C, Xie Y, Cai Y, Wang S, Gao J, Ni Q, Yao J (2018) Flexible and porous cellulose
352 aerogels/zeolitic imidazolate framework (ZIF-8) hybrids for adsorption removal of Cr(IV) from
353 water. *Journal of Solid State Chemistry* 262:135-141

354 Chan WH, Mazlee MN, Ahmad ZA, Ishak M, Shamsul JB (2015) The development of low cost
355 adsorbents from clay and waste materials: a review. *Journal of Material Cycles and Waste*
356 *Management* 19:1-14

357 Chen JP, Lin M (2001) Equilibrium and kinetics of metal ion adsorption onto a commercial H-type
358 granular activated carbon: experimental and modeling studies. *Water Research* 35:2385-2394

359 Chen S, Wei S, Feng Y, Hu W, Wang H (2010) Preparation of amidoximated bacterial cellulose and its
360 adsorption mechanism for Cu^{2+} and Pb^{2+} . *Journal of Applied Polymer Science* 117:8-15

361 Chen S, Yu Z, Yan Z, Wei S, Shi S, Xiang Z, Wang H (2009) Carboxymethylated-bacterial cellulose for
362 copper and lead ion removal. *Journal of Hazardous Materials* 161:1355-1359

363 Da Silva Pinto M, Sierra-Avila CA, Hinestroza JP (2012) In situ synthesis of a Cu-BTC metal-organic
364 framework (MOF 199) onto cellulosic fibrous substrates: cotton. *Cellulose* 19:1771-1779

365 Fei J, Li C, Bo T, Xu J, Peng L (2012) Preparation of cellulose acetate/zeolite composite fiber and its
366 adsorption behavior for heavy metal ions in aqueous solution. *Chemical Engineering Journal*
367 209:325-333

368 Furukawa H, Cordova KE, O'Keeffe M, Yaghi OM (2013) The chemistry and applications of metal-
369 organic frameworks. *Science* 341:974

370 Gurgel L, Freitas R, Gil LF (2008) Adsorption of Cu(II), Cd(II), and Pb(II) from aqueous single metal
371 solutions by cellulose and mercerized cellulose chemically modified with succinic anhydride.
372 *Carbohydrate Polymers* 74:922-929

373 Ha H, Shanmuganathan K, Ellison CJ (2015) Mechanically stable thermally crosslinked poly(acrylic
374 acid)/reduced graphene oxide aerogels. *ACS Appl Mater Interfaces* 7:6220-6229

375 Hu Y, Kazemian H, Rohani S, Huang Y, Song Y (2011) In situ high pressure study of ZIF-8 by FTIR
376 spectroscopy. *Chemical Communications* 47:12694-12696

377 Huang H, Yu Y, Qing Y, Xiaofeng Z, Cui J, Wang H (2020) Ultralight Industrial Bamboo Residue-
378 Derived Holocellulose Thermal Insulation Aerogels with Hydrophobic and Fire Resistant Properties.
379 *Materials* 13:477

380 Isogai A, Saito T, Fukuzumi H (2011) TEMPO-oxidized cellulose nanofibers. *Nanoscale* 3:71-85

381 Jia YF, Xiao B, Thomas KM (2002) Adsorption of Metal Ions on Nitrogen Surface Functional Groups in
382 Activated Carbons. *Langmuir* 18:470-478

383 Oh SY, Yoo DI, Shin Y, Kim HC, Kim HY, Chung YS, Park WH, Youk JH (2005) Crystalline structure
384 analysis of cellulose treated with sodium hydroxide and carbon dioxide by means of X-ray
385 diffraction and FTIR spectroscopy. *Carbohydrate research* 340:2376-2391

386 Pan Y, Liu Y, Zeng G, Zhao L, Lai Z (2011) Rapid synthesis of zeolitic imidazolate framework-8 (ZIF-
387 8) nanocrystals in an aqueous system. *Chemical Communications* 47:2071-2073

388 Peng F, Sun RC (2010) Modification of Cereal Straws as Natural Sorbents for Removing Metal Ions
389 from Industrial Waste Water - ScienceDirect. *Cereal Straw as a Resource for Sustainable*
390 *Biomaterials and Biofuels*:219-237

391 Song W, Zhu M, Zhu Y, Zhao Y, Yang M, Miao Z, Ren H, Ma Q, Qian L (2020) Zeolitic imidazolate
392 framework-67 functionalized cellulose hybrid aerogel: an environmentally friendly candidate for
393 dye removal. *Cellulose* 27:2161-2172

394 Tran A, Pham TT, Nguyen QH, Hoang N, Bruggen B (2020) From waste disposal to valuable material:
395 Sulfonating polystyrene waste for heavy metal removal. *Journal of Environmental Chemical*
396 *Engineering* 8:104302

397 Wang L, Xu H, Gao J, Yao J, Zhang Q (2019) Recent progress in metal-organic frameworks-based
398 hydrogels and aerogels and their applications. *Coordination Chemistry Reviews* 398:213016

399 Wang M, Chen Y, Qin Y, Wang T, Yang J, Xu F (2019) Compressible, Fatigue Resistant, and Pressure-
400 Sensitive Carbon Aerogels Developed with a Facile Method for Sensors and Electrodes. *ACS*
401 *Sustainable Chemistry & Engineering* 7:12726-12733

402 Wang M, Shao C, Zhou S, Yang J, Xu F (2017) Preparation of carbon aerogels from TEMPO-oxidized
403 cellulose nanofibers for organic solvents absorption. *RSC Advances* 7:38220-38230

404 Yan J, Huang Y, Miao Y-E, Tjiu WW, Liu T (2015) Polydopamine-coated electrospun poly(vinyl
405 alcohol)/poly(acrylic acid) membranes as efficient dye adsorbent with good recyclability. *Journal*
406 *of Hazardous Materials* 283:730-739

407 Yang Q, Lu R, Ren S, Chen C, Chen Z, Yang X (2018) Three dimensional reduced graphene oxide/ZIF-
408 67 aerogel: Effective removal cationic and anionic dyes from water. *Chemical Engineering Journal*
409 348:202-211

410 Yang Q, Ren S, Zhao Q, Lu R, Hang C, Chen Z, Zheng H (2018) Selective separation of methyl orange
411 from water using magnetic ZIF-67 composites. *Chemical Engineering Journal* 333:49-57

412 Yichang P (2011) Rapid synthesis of zeolitic imidazolate framework-8 (ZIF-8) nanocrystals in an
413 aqueous system. *Chemical communications* (Cambridge, England) 7
414 Zhang C, Zhang RZ, Ma YQ, Guan WB, Wu XL, Liu X, Li H, Du YL, Pan CP (2015) Preparation of
415 Cellulose/Graphene Composite and Its Applications for Triazine Pesticides Adsorption from Water.
416 *Acs Sustainable Chemistry & Engineering* 3:396-405
417 Zhao D, Zhu Y, Cheng W, Chen W, Wu Y, Yu H (2020) Cellulose-Based Flexible Functional Materials
418 for Emerging Intelligent Electronics. *Adv Mater*:e2000619
419 Zhou S, Kong X, Zheng B, Huo F, Strømme M, Xu C (2019) Cellulose Nanofiber @ Conductive Metal-
420 Organic Frameworks for High-Performance Flexible Supercapacitors. *ACS Nano* 13:9578-9586
421 Zhu L, Zong L, Wu X, Li M, Wang H, You J, Li C (2018) Shapeable Fibrous Aerogels of Metal-Organic-
422 Frameworks Templated with Nanocellulose for Rapid and Large-Capacity Adsorption. *ACS Nano*
423 12:4462-4468
424

Supplementary Files

This is a list of supplementary files associated with this preprint. Click to download.

- [MovieS1.mp4](#)
- [MovieS2.mp4](#)
- [MovieS3.mp4](#)
- [MovieS4.mp4](#)
- [supportinginformation.docx](#)